



Features and sources of aerosol properties over the western Pacific Ocean based on shipborne measurements

Weibo Wang^{1,2} · Chunsheng Jing^{1,2} · Dayong Zhu^{1,2} · Xiaogang Guo^{1,2}

Received: 5 October 2022 / Accepted: 10 March 2023 / Published online: 7 April 2023
© The Author(s), under exclusive licence to Springer-Verlag GmbH Austria, part of Springer Nature 2023

Abstract

In the Western Pacific, the limited in situ observations of aerosol optical depth (AOD) show substantial north–south differences in its spectral distribution, magnitude, seasonal fluctuation, and Angstrom exponent. Two sets of observation data collected in spring 2017 and summer 2019 are used to investigate aerosol size distribution and its sources through the GRASP (Generalized Retrieval of Aerosol and Surface Properties) inversion method and HYSPLIT (HYbrid Single-Particle Lagrange Integrated Trajectory) particle trajectories model. The retrieved aerosol size distribution (normalized by aerosol volume concentration) is homogeneous over the western Pacific Ocean. The aerosol volume concentration ($C_{v,c}$) in the coarse mode is substantially higher than that in the fine mode ($C_{v,f}$) in this region, indicating that coarse particles predominate. The northernmost section has the highest $C_{v,f}$ with an average value of 0.04, which is 4.5 times that of the other sections except the sites observed in 2019, because of the Long-Range Transport (LRT) of dust from the Gobi and Mongolian Plateau. The equatorial section has the highest $C_{v,c}$ with an average value of 0.22 for the coarse mode, which is 1.5–3 times higher than that of the other section. Its single scattering albedo (SSA) is the smallest in all sections ($SSA(440)=0.95$). Analysis displays that the section is affected by elevated-smoke and polluted-continental/smoke types due to the biomass burning around Papua New Guinea. In addition, an AOD(500) with a value of 0.048, which is lower than the traditional oceanic AOD baseline, is obtained in summer 2019. In comparison to it, the projected net shortwave and longwave radiative effect of spring observed LRT high concentration PM_{10} plume ($AOD(550)=0.09$) from Southeast Asia at the sea surface are -3.1 W m^{-2} and -1.4 W m^{-2} under clear sky conditions, resulting in a net radiative effect of -1.7 W m^{-2} . As the cold surge frequency increases due to the warming Arctic, more LRT events may be expected as a result of climate change.

1 Introduction

Aerosol, which is made up of small solid and liquid particles dispersed and suspended in the gas from both natural and anthropogenic sources (Wang et al. 2007; Wang et al. 2022), can disrupt the atmospheric radiation balance by interacting with solar and terrestrial radiation (Ramanathan et al. 2001; Zhao et al. 2020) and changing cloud properties and

lifetimes (Twomey 1977; Kaufman et al. 2002; Garrett and Zhao 2006; Zhao et al. 2018a; Yang et al. 2021), further modifying the radiation budget of the Earth-atmosphere system (Dubovik et al. 2000; Yang et al. 2021). The variation in atmospheric loading of aerosols has a substantial impact on the climate system's radiation balance and cloud process. Dust and black carbon aerosols can absorb substantial amounts of solar radiation and subsequently heat the atmosphere directly (Sun and Zhao 2020). Marine aerosols containing organic and sea salt contents strongly influence the radiative coupling between ocean and atmosphere by scattering and absorbing solar radiation, thereby affecting the climate system and atmospheric environment (Eck et al. 2005; Sakerin et al. 2008; Zhao et al. 2020), highlighting the vital need for research into the origin of aerosols and their temporal variation, as well as their transport pathways in the atmosphere (Alizadeh-Choobari et al. 2014).

Aerosol Optical Depth (AOD) refers to the integral of aerosol attenuation coefficient from the top of the atmosphere

Responsible Editor: Clemens Simmer, Ph.D.

✉ Weibo Wang
wangwb@tio.org.cn

¹ Ocean Dynamic Laboratory, Third Institute of Oceanography, Ministry of Natural and Resources, Xiamen 361005, People's Republic of China

² Fujian Provincial Key Laboratory of Marine Physical and Geological Processes, Xiamen 361005, People's Republic of China

to the surface (King et al. 1978; Wang et al. 2022). In addition to being a crucial physical parameter for characterizing atmospheric turbidity (Aoki and Fujiyoshi 2003), AOD plays a significant factor in determining how aerosols affect the climate. Typically, AOD is low over the open ocean (< 0.1 in the midvisible [e.g., Smirnov et al. 2011, 2009]). The AOD may exceed 1 in the midvisible under the influence of dust events in East Asia [e.g., (Eck et al. 2005; Han et al. 2012)]. Dust events are more common over Taklimakan but less frequent and more intense throughout the Gobi Desert, maintaining a height between 2.5–4.0 km and being transported across eastern China and over the Pacific Ocean by upper tropospheric westerly jets (Huang et al. 2009). Zhang et al. (1997) reported that the emission intensity of Asian dust aerosol is approximately 800 Tg a^{-1} , of which approximately 30% will resettle in the desert area, 20% of the dust particles can be transported between regions, and the remaining approximately 50% of the dust particles can be transported to the Western Pacific or even further away. In East Asia, high-density aerosols happen in the local troposphere as a result of the harsh dust weather, high population density, and high oil–gas consumption caused by active economic activities (Eck et al. 2005; Han et al. 2012; Li and Han 2016; Li et al. 2016; Lee et al. 2020). Mixing dust aerosols with marine aerosols results in more complex physical and optical properties of aerosols, which leads to great uncertainties in climate predictions (Tian et al. 2019).

In the northwest Pacific Ocean, there is a strong seasonal cycle, which is most pronounced in the monthly AOD averages (Husar et al. 1997; Alizadeh-Choobari et al. 2014). AOD reaches its peak between March and May (Eck et al. 2005). A continuous meridional study on AOD over the Western Pacific Ocean reveals some notable north–south differences with a border of 25°N , including its spectral distribution, the magnitude of AOD, Ångström Index, and seasonal fluctuation (Wang et al. 2022). Wang et al. (2022) proposed that the barrier of subtropical high (SH) results in a north–south disparity. The spring peak in the north is caused by long-range transport (LRT) of dust associated with the permanent SH. In terms of climatology, the site of the AOD(630) maximum approximately 35°N advances northward by 10.5° as the SH ridge moves northward up to 12° from February to August.

There is scant research on the north–south differential in aerosol characteristics and the extent of LRT of pollutants to the Western Pacific due to the limitations of field studies in temporal and geographical range. Wang et al. (2022) preliminarily reported the north–south difference in AOD and its spectral distribution over the Western Pacific. Aerosol characteristics and potential sources are not mentioned. In addition, Sayer et al. (2012) retrieved the maritime aerosol volume size distribution from 11 Aerosol Robotic Network (AERONET) island sites distributed throughout the world's

oceans, as a foundation for defining such a model for pure (polluted) maritime aerosol. Therefore, the research also includes the retrieval and comparison of aerosol volume size distribution from the observation AOD based shipborne measurements in the Western Pacific. The aim of the present study is twofold: (1) The north–south differences of aerosol properties, including aerosol volume size distribution ($\frac{dV(r)}{d\ln(r)}$), aerosol volume concentration (C_v) and single scattering albedo (SSA) retrieved from shipborne observation AOD, are discussed; (2) The sources and mechanism of aerosol LRT to the Western Pacific are investigated. Meanwhile, we also estimate the clear sky direct radiative forcing effect of the LRT aerosols over the Western Pacific Ocean using the Fu-Liou radiative transfer model. This paper is organized as follows: the next section describes the observation data, modelling and methodology used in the analysis. The results are presented in the third section followed by a brief discussion and are then summarized in the final section.

2 Materials and methods

2.1 Materials

The AOD observation were carried out in the Western Pacific Ocean by the project “Global changes and Air-Sea Interaction I (GASI I)” from April to May 2017. We hold a Microtops II solar photometer produced by Solar Light company to measure AOD at 440 nm, 500 nm, 675 nm, 870 nm and 1020 nm. In the observation region, the latitude span of the observed sea area is more than 40° . Another project “Global changes and Air-Sea Interaction II (GASI II)” conducted a zonal section near 25°N with a longitude span of 28° at the end of August 2019. The observation equipment is the same as that in 2017. Figure 1 depicts the specific observation stations. The evidence of the north–south difference of AOD involving the spectrum and the derived Ångström exponent implies that the meridional section should be segmented according to 25°N (Wang et al. 2022). The GASI I meridional stations are divided into two sections, which are represented by the pink line (high latitude) and green line (middle-low latitude). In Fig. 1, the 25°N zonal section is represented by the orange line, while the 0° section is represented by the blue line.

We took 15 successive observations within 3 min at each station to prevent measurement bias due to the thin cloud and ship shaking. All 15 observations were conducted in the presence of apparent direct sunshine. We eliminate observation recordings whose data are considerably anomalous during postprocessing owing to various events, such as the ship's tail smoke. Then, the observation value was calculated by averaging the remaining data.

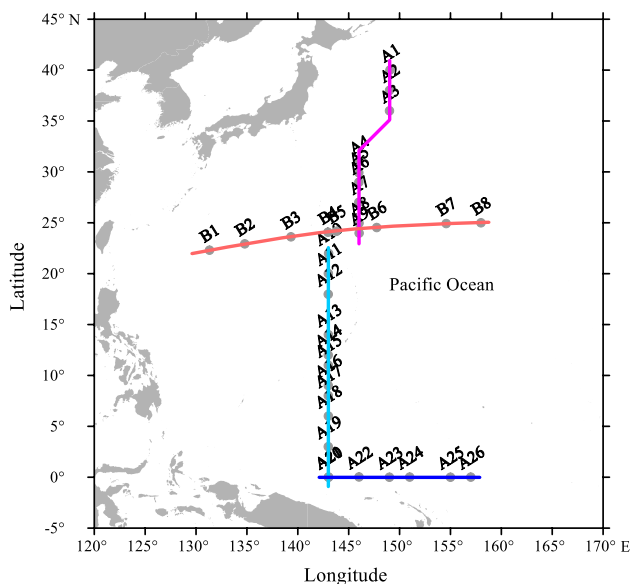


Fig. 1 The field observation stations in GASI I and GASI II. All stations are divided into four sections S1, S2, S3, and S4, denoted by red, green, blue, and orange solid lines, respectively

The wind dataset at 10 m above sea level derived from the Copernicus Marine Service conducted in the European Union’s Earth Observation Programme is chosen for acquiring wind history speed (WHS) (detailed information is on the website: https://data.marine.copernicus.eu/product/WIND_GLO_PHY_L4_MY_012_006/description), which is defined by repeating the procedure backward in 6 h increment, and averaging the resulting wind speed for up to 24/96 h prior to the observation datetime (Sayer et al. 2012). It is performed for each synoptic time (00:00; 06:00; 12:00; 18:00) and with a spatial resolution of 0.25° in longitude and latitude over the global ocean. In the paper, the optimal neighborhood interpolation method is used to acquire the WHS in observation sites.

The remote sensing results of the vertical distribution of aerosol types were derived from the Cloud-Aerosol Lidar and Infrared Pathfinder Satellite Observation (CALIPSO) satellite (<https://eosweb.larc.nasa.gov/project/calipso>) (Winker et al. 2007). The Vertical Feature Mask (VFM) level 2 version 4.20 data were used to analyze the aerosol types transported to the observation sites (Fig. 1). The VFM products contained the aerosol classifications of clean/dusty marine aerosol, pure/polluted dust, clean/polluted continental, and smoke. Detailed information about the classification algorithm is shown in the literature(Winker et al. 2009).

2.2 GRASP algorithm

The measurements at 440, 500, 675, 870 and 1020 nm were used to retrieve aerosol volume size distribution following the methodology of Generalized Retrieval of Aerosol and Surface Properties (GRASP), which implements statistically optimized fitting of diverse observations using multiterm least square method concept (Torres et al. 2017). Correspondingly, the retrieval is organized as a solution search in the continuous space of solutions without the traditional use of precalculated look-up tables. The GRASP algorithm is highly versatile and can be applied to a large variety of remote sensing measurements (Torres et al. 2017), such as, sun photometer (Li et al. 2019, 2022), lidars (Chen et al. 2020; Lopatin et al. 2021), satellite imagers (Roman et al. 2022), etc. .

Here, in the GRASP algorithm, the particle size distribution is characterized as bimodal log-normal (Fine and Coarse), and the refractive index (m) is assumed to be known. Observational evidence suggests that the fine mode is composed largely of sulfates, organic compounds, and salt, while the coarse mode is predominantly salt. The different compositions would be expected to lead to different refractive indices for the two modes. The recommended refractive index (fine mode $m = 1.415 - 0.002i$, coarse mode $m = 1.363 - 3 \times 10^{-9}i$) is used in Sayer et al. (2012), independent of the wavelength.

Frequently used metrics to characterize aerosol size distributions include the logarithmic volume median radius (r_v) as a measure of the size of the aerosol particles for both fine and coarse modes (Sayer et al. 2012), where

$$\ln(r_v) = \frac{\int_{r_{\min}}^{r_{\max}} \ln(r) \frac{dV(r)}{d\ln(r)} d\ln(r)}{\int_{r_{\min}}^{r_{\max}} \frac{dV(r)}{d\ln(r)} d\ln(r)}, \tag{1}$$

and the geometric standard deviation (σ) of the distribution for the volume median radius (Sayer et al. 2012):

$$\sigma_v = \sqrt{\frac{\int_{r_{\min}}^{r_{\max}} (\ln(r) - \ln(r_v))^2 \frac{dV(r)}{d\ln(r)} d\ln(r)}{\int_{r_{\min}}^{r_{\max}} \frac{dV(r)}{d\ln(r)} d\ln(r)}} \tag{2}$$

The aerosol volume concentration (C_v) is,

$$C_v = \int_{r_{\min}}^{r_{\max}} \frac{dV(r)}{d\ln(r)} d\ln(r). \tag{3}$$

The median radius of the number distribution r_n is defined analogously to Eq. (3), using number size distribution ($\frac{dN(r)}{d\ln(r)}$) in place of $\frac{dV(r)}{d\ln(r)}$. A third useful quantity is the effective radius (r_{eff}), the ratio of the third to second moments of the number size distribution (Sayer et al. 2012):

$$r_{\text{eff}} = \frac{\int_{-\infty}^{+\infty} r^3 \frac{dN(r)}{d\ln(r)} d\ln(r)}{\int_{-\infty}^{+\infty} r^2 \frac{dN(r)}{d\ln(r)} d\ln(r)} \quad (4)$$

In this context, the subscripts *f* and *c* are used to distinguish fine mode and coarse mode.

2.3 HYSPLIT

Hybrid Single-Particle Lagrangian Integrated Trajectory (HYSPLIT) is a complete system for computing simple air parcel trajectories, as well as complex transport, dispersion, chemical transformation, and deposition simulations. The model calculation method is a hybrid between the Lagrangian approach, using a moving frame of reference for the advection and diffusion calculations as the trajectories or air parcels move from their initial location, and the Eulerian methodology, which uses a fixed three-dimensional grid as a frame of reference to compute pollutant air concentrations (Stein et al. 2015; Rolph et al. 2017).

The averaged wind speed data was used in the calculation of 120 h backward trajectory data and produced by the National Centers for Environmental Prediction Global Data Assimilation System (GDAS 0.5°). The vertical transport was modeled using the Model Vertical Velocity option of HYSPLIT. The back trajectories were computed every 6 h at 100 m, 2000 m and 5000 m above sea surface.

2.4 Fu-Liou radiative transfer model

The Fu-Liou radiative transfer model (RTM) is used to estimate the radiative forcing impact of observed aerosols. It is a delta-four stream solver with 15 shortwave and 12 longwave spectral bands (Qiang Fu and Liou 1992, 1993). The “Mid-LatSummer” standard atmosphere, “IGBP” Surface Albedo, and “17 Ocean” spectral distribution options were chosen. In this study, the observed column aerosol optical depth (AOD) was used to calculate the clear sky (cloud free) aerosol net direct radiative forcing effect.

3 Result

In fact, the lack of scattering information in the AOD observation results in the necessity of using a priori constraints. The GRASP algorithm was described using bimodal log-normal size distributions and a priori estimates of refractive indices and sphericity parameters (Torres et al. 2017). Some validations of the GRASP algorithm have been done through a comparison with the aerosol properties obtained from the AERONET standard inversion and have shown that spectral AOD measurements are sufficient for a precise discrimination between the extinction of the fine and coarse

modes, independent from any assumption (Dubovik et al. 2000, 2002; Dubovik and King 2000; Torres et al. 2017). Given that there are few observations for marine aerosols and that the observed AOD is significantly smaller than that of terrestrial aerosols, some of which are even less than 0.1, it is necessary to represent the error of AOD obtained by GRASP.

3.1 The relative error of the retrieved AOD in GRASP

The comparison between the simulated AOD from GRASP and the shipborne measurement result is performed at six typical sites distributed across four sections. The observed AOD of A1 is generally comparable with the simulated AOD (in Fig. 2), and the relative error (RE) is only 5.45%. Only 6.39% on average is the RE over S1 (in Table 1). The RE in S2 section A5 is 14.47%, and the highest RE in this section is in A20 at 25.3%. The average RE in S2 is 16.07%. The RE of A23 in the S3 section is just 5.55%, which is the lowest in this section. Only 8.28%, or close to that of S1 is average in S3. The REs of B1 and B5 are 9.13% and 29.03%, respectively, in the S4 section, with B5 being the greatest of all sites. The average RE is 18.93% in S4. Except for B5, where the RE is somewhat higher than that of S2, the average RE is 17.49%. Figure 3 depicts out analysis of the relationship between all observed AOD (440) and RE. The RE is generally less than 5% when AOD (440) is more than 0.2. The RE substantially rises with the decrease in AOD (440) once AOD (440) is less than 0.2.

In general, the base AOD for the calmest waters appears to be 0.068 at 440 nm, 0.065 at 500 nm, and 0.035 at 1020 nm. Kaufman et al. (2001) reported that the ‘baseline maritime’ AOD at 500 nm is of order 0.053–0.071. Note that in the Western Pacific, under the control of the subtropical high, we even observed that the AOD (500) is only 0.048 in B6, which is lower than previous reports.

The Western Pacific exhibits a clear north–south difference in AOD spectral distribution. The AOD spectral distribution shows declines with increasing wavelength at sites north of 25 °N (Wang et al. 2022), and the inversion spectrum of AOD agrees well with the measured spectrum (such as A1 in Fig. 2a). However, for sites south of 25 °N, the measured AOD reaches a high value at 500 nm (Wang et al. 2022). The inversion spectrum still shows monotonically decreasing characteristics, and there is a large error with the measured spectrum (such as A15, A20, A23, B1, and B5 in Fig. 2).

Dubovik et al. (2011) assessed the accuracy of the inversion algorithm for deriving aerosol optical properties from Sun-sky radiance measurements, and observed a particularly distinct increase in errors with decreasing AOD. Indeed, Fig. 2 shows that the inaccuracy is considerably raised with a tiny AOD. A diagnostic analysis conducted by Dubovik

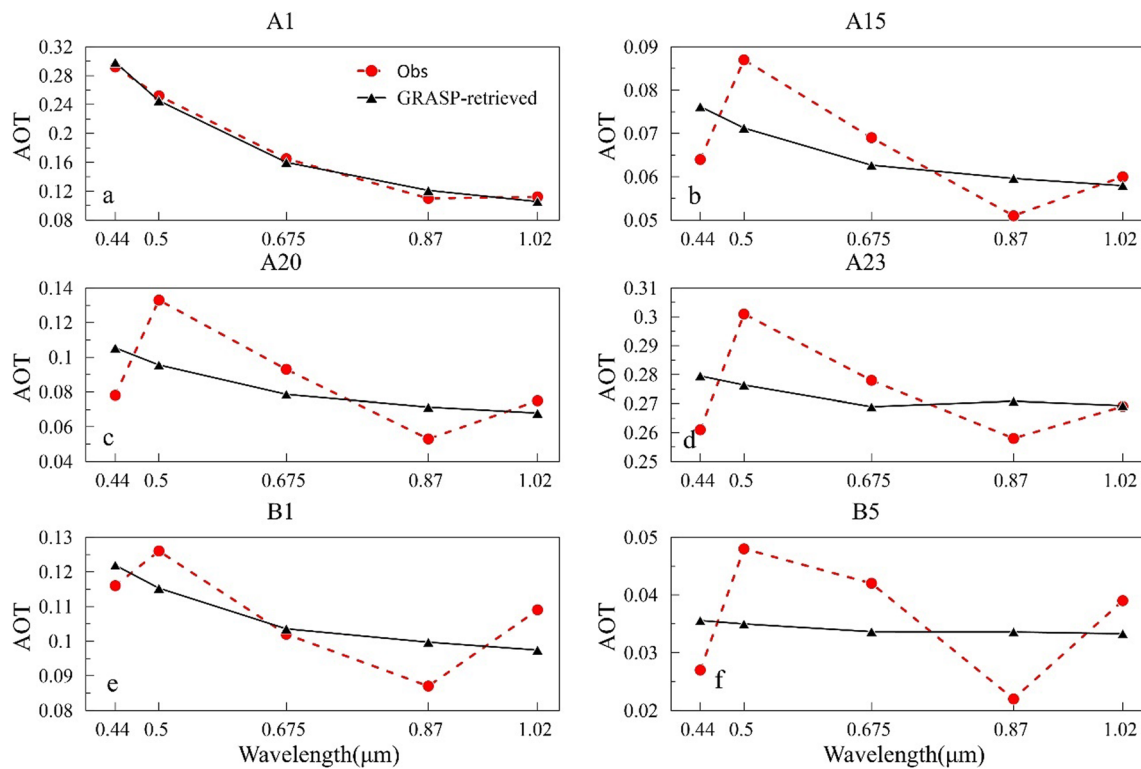


Fig. 2 Comparisons of the retrieved AOD from the GRASP algorithm with the field observation AOD in A1, A15, A20, A23, B2, and B6

Table 1 Description of aerosol properties retrieved from the GRASP algorithm, including the relative error (RE), and the size distribution (modeled as a bimodal log-normal function: $r_{v,i}$ (μm), σ_i and $r_{\text{eff},i}$ (μm))

SEC	S1	S2	S3	S4
RE (%)	6.390	16.070	8.280	18.930
$r_{v,f}$	0.151	0.155	0.148	0.152
σ_f	0.407	0.411	0.403	0.406
$r_{v,c}$	3.154	3.154	3.154	3.152
σ_c	0.701	0.703	0.701	0.702
$r_{\text{eff},f}$	0.140	0.143	0.137	0.140
$r_{\text{eff},c}$	2.451	2.446	2.450	2.448
$r_{\text{eff},t}$	0.626	1.091	1.479	1.402

The refractive index (fine mode $m=1.415-0.002i$, coarse mode $m=1.363-3 \times 10^{-9}i$) is recommended for Marine Aerosol in Sayer et al. (2012). Note that the values of the sphericity parameter (Sph) are constant with a value of 100. The subscripts f and c denote the fine mode and coarse mode, respectively

et al. (2000) reveals that the considerable inaccuracies are caused by no complete independence of the scattering effect between the real and imaginary parts of the complex refractive index. Torres et al. (2017) particularly emphasized that the characterizations of aerosol fine-mode optical properties retrieved from GRASP are accurate, even though they

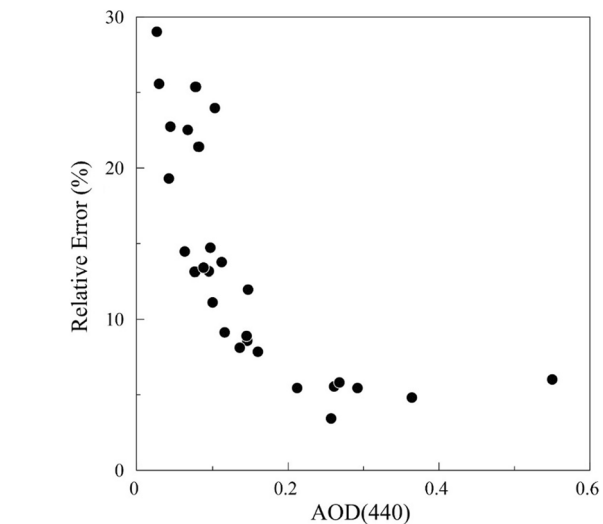


Fig. 3 The relationship between the observation AOD (440) and Relative Error

rely on reliable a priori information about the real refractive indices and accurate measurement of AOD. The uncertainty for the fine mode $r_{v,f}$ and $C_{v,f}$ ranges between 5% for the cases with a fine-mode predominance and 10% for the cases with a prevailing coarse mode. The characterization of the optical properties of the coarse mode is less accurate but can be

significantly improved using moderate a priori information about coarse-mode parameters. Torres et al. (2017) even advocate a lower limit of $AOD(440) = 0.2$ for the bimodal size distribution parameters to ensure quality retrievals of aerosol optical properties.

In fact, the retrieval of the particle volume size distribution was demonstrated to be adequate in practice [e.g., $AOD(440) \geq 0.05$], as demonstrated by Dubovik et al. (2000). Several scientists have applied the algorithm to observation data less than 0.2 (e.g., Dubovik and King 2000; Dubovik et al 2000; Sayer et al. 2012). The following research shows that the retrieved aerosol volume size distribution (normalized by particle volume concentration C_v) is universal

and that the difference between all stations is negligible. As a result, we believe that the GRASP algorithm can meet the needs of research on aerosol properties in the Western Pacific.

3.2 Aerosol volume size distribution over the Western Pacific Ocean

Figure 4 shows the parameters associated with the bimodal volume particle size distribution. In specific, for each mode of the volume particle size distribution, we computed volume median radius (r_v), standard deviation (σ), effective radius (r_{eff}), aerosol volume concentration (C_v), and aerosol

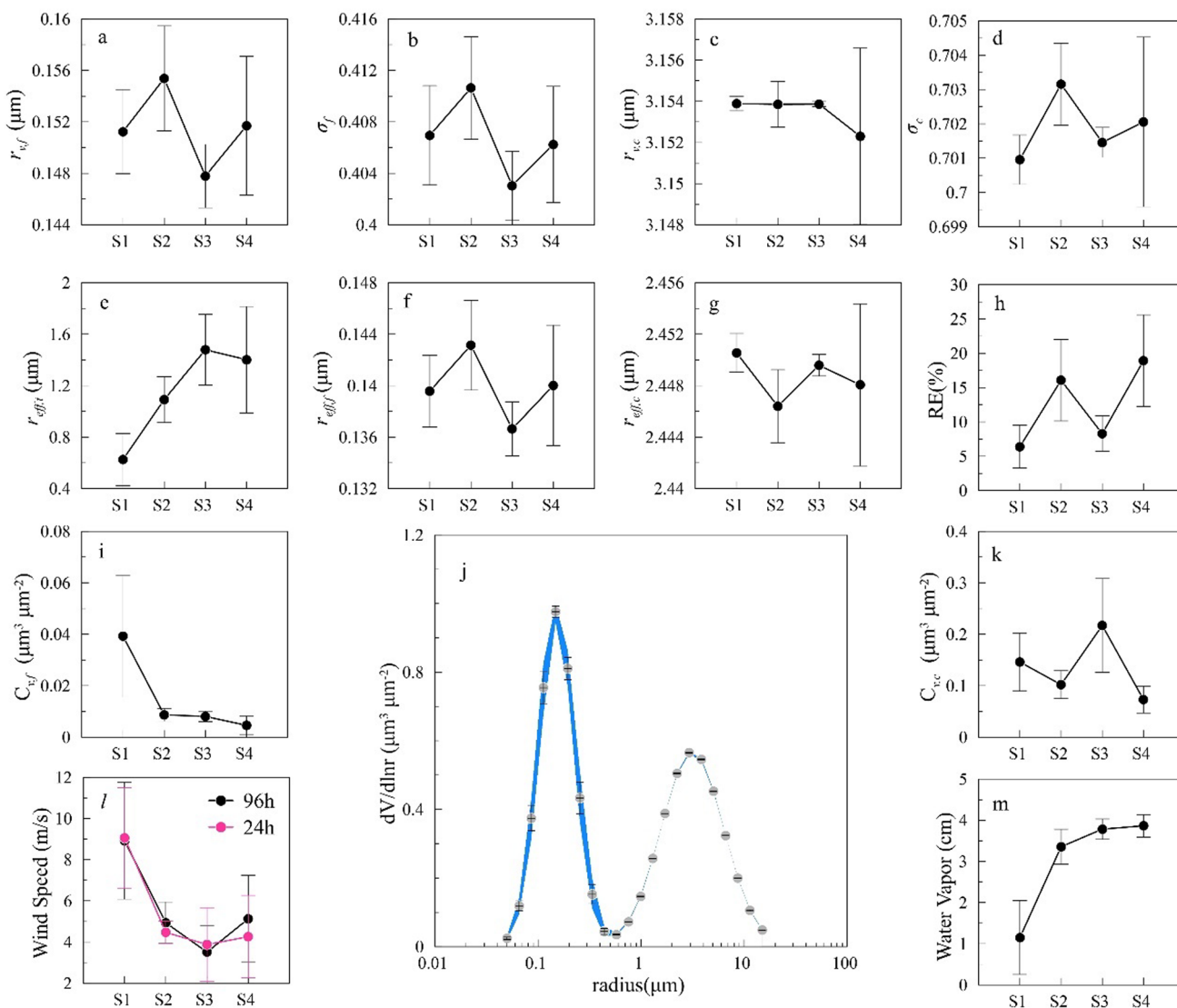


Fig. 4 The average aerosol optical properties retrieved from GRASP, including volume median radius (r_v) (a, c), standard deviation (σ) of the distribution for the volume median radius (b, d), effective radius (r_{eff}) (e, f, g), relation error (RE) (h), aerosol volume concentration (C_v) (i, k), and aerosol volume size distribution (j) normalized by aer-

osol volume concentration (C_v). Using subscripts f and c distinguish fine-mode and coarse-mode. The subscript t in e denotes the total effective radius. In j, the blue region denotes the range of $dV(r)/dln(r)$. The gray dots represent the 22 logarithmically-spaced size bins on the retrieved optical properties denote the standard deviation

volume size distribution ($\frac{dV(r)}{d\ln(r)}$) normalized by aerosol volume concentration using the GRASP algorithm. The average value and standard deviation for these parameters (decomposed into fine-mode and coarse-mode) for 4 sections are shown as well.

In the algorithm, all particles with radii smaller than 0.6 μm are classified as fine mode, while all particles with radii larger than 0.6 μm belong to coarse mode. Although the average RE range for the four sections is 5 ~ 20%, the retrieved particle volume size distribution parameters, including r_v and σ , are consistent even for low aerosol loading (Fig. 4a–d). All sites show a homogeneous bimodal volume distribution, with a fine mode peaking at 0.1–0.2 μm and a coarse mode peaking near 3 μm (in Fig. 4j), in accordance with the observation results in Sayer et al. (2012) at island sites spanning a variety of oceans. The retrieved particle volume size distribution illustrates the domination of large sea-salt particles in oceanic aerosols ($C_{v,c} > C_{v,f}$).

Table 2 presents parameters of the mean bimodal log-normal size distribution, including r_v , r_{eff} , and σ . Compared with the pure (unpolluted) marine aerosol volume size distribution revealed by Sayer et al. (2012), the difference in parameters between the two is modest. In terms of the fine mode, $r_{v,f}$, $r_{\text{eff},f}$ and σ_f are practically the same. In contrast, in coarse mode, there exists a tiny difference between the two. Retrieved values for the coarse mode are more comparable to the observation data at Nauru Island located on the equator of the Western Pacific Ocean. In general, the particle volume size distribution in the Western Pacific collected from shipborne observation AOD is similar to the prior observation results (e.g. Simronv et al. 2011; Sayer et al. 2012), showing a relatively modest retrieval standard deviation, indicating a strong stability of our results. The broad resemblance is an indicator of the comparable sources of the aerosol at different sites.

Table 2 The aerosol optical properties for use in aerosol size distribution

Parameter	Value		
	Sayer et al. (2012)	In Paper	Nauru
Fine Mode			
$r_{v,f}$	0.157 μm	0.152 μm	0.174 μm
$r_{\text{eff},f}$	0.139 μm	0.140 μm	0.149 μm
σ_f	0.50	0.407	0.55
Coarse Mode			
$r_{v,c}$	2.59 μm	3.153 μm	2.94 μm
$r_{\text{eff},c}$	2.00 μm	2.449 μm	2.34 μm
σ_c	0.72	0.702	0.67

Sayer et al (2012)’s observation results at island sites spanning a variety of oceans are compared

Changes in aerosol volume size distribution are primarily responsible for variations in the volume concentration over the Western Pacific. In the fine mode, a significant increase in $C_{v,f}$ with an average value of 0.0393 is seen in the fine mode due to some influence of the LRT of Asian dust and pollution in S1. It is 4.5 times the average value at S2 and S3, and 8.5 times that at S4 with a lowest value of 0.0046. Because the size distribution in fine mode is unaffected by wind speed, relative humidity, and columnar water vapor in unpolluted maritime conditions, $C_{v,f}$ can be used to estimate the maritime AOD and Angström exponent. The average value of $C_{v,f}$ at S2, S3 and S4 is essentially consistent with the constant $C_{v,f}$ of 0.0057 proposed by Sayer et al. (2012). The change in $C_{v,f}$ is considered to be modest, but potentially decreased as wind speeds increase. Without taking S1 into account, $C_{v,f}$ appears to have a weak negative association with wind speed in this research as well.

Meteorological factors such as wind speed and moisture availability influence oceanic aerosol loading(Eck et al. 2009; Sayer et al. 2012; Merkulova et al. 2018). The most evident is that there is a clear positive association between wind speed history (WSH) and $C_{v,c}$ for the coarse mode except for the S3 section. Figure 5i demonstrates that $C_{v,c}$ over S1 is noticeably higher than those over S2 and S4, and WSH over S1 is likewise higher than those over S2 and S4. The average $C_{v,c}$ at S3 is the highest of all sections, and the accompanying WSH and water vapor content (in Fig. 5m) are not obviously higher. To explain this inconsistency, in the next section, we will analyze the difference in aerosol types between the four sections from satellite remote sensing data.

3.3 The north–south difference in aerosol types over the Western Pacific Ocean

Since the CALIPSO satellite employed lidar to determine the vertical distribution of aerosol types (VFM dataset) with a high resolution, we cannot obtain the horizontal distribution for the entire observation region. Only four tracks passing through the observation station were chosen from April to May 2017, which were made on April 19, April 30, May 7, and May 9, 2017, to demonstrate the north–south difference in aerosol types in the Western Pacific.

orth of 25 °N over the Western Pacific, the aerosol types spanning in 0 ~ 8 km include clear marine (CM), dust (DU), polluted dust (PD), elevated smoke (ES), and dusty marine (DM) aerosols. A dust plume with a range of 3 ~ 8 km has been observed, with the potential of originating from the mainland of East Asia, which is home to some of the largest and most persistent dust sources in the northern hemisphere. The sizes of dust gets shifted to finer size thousands of kilometers away from where they originated, resulting in $C_{v,f}$ being substantially greater in this region than in the mid-low

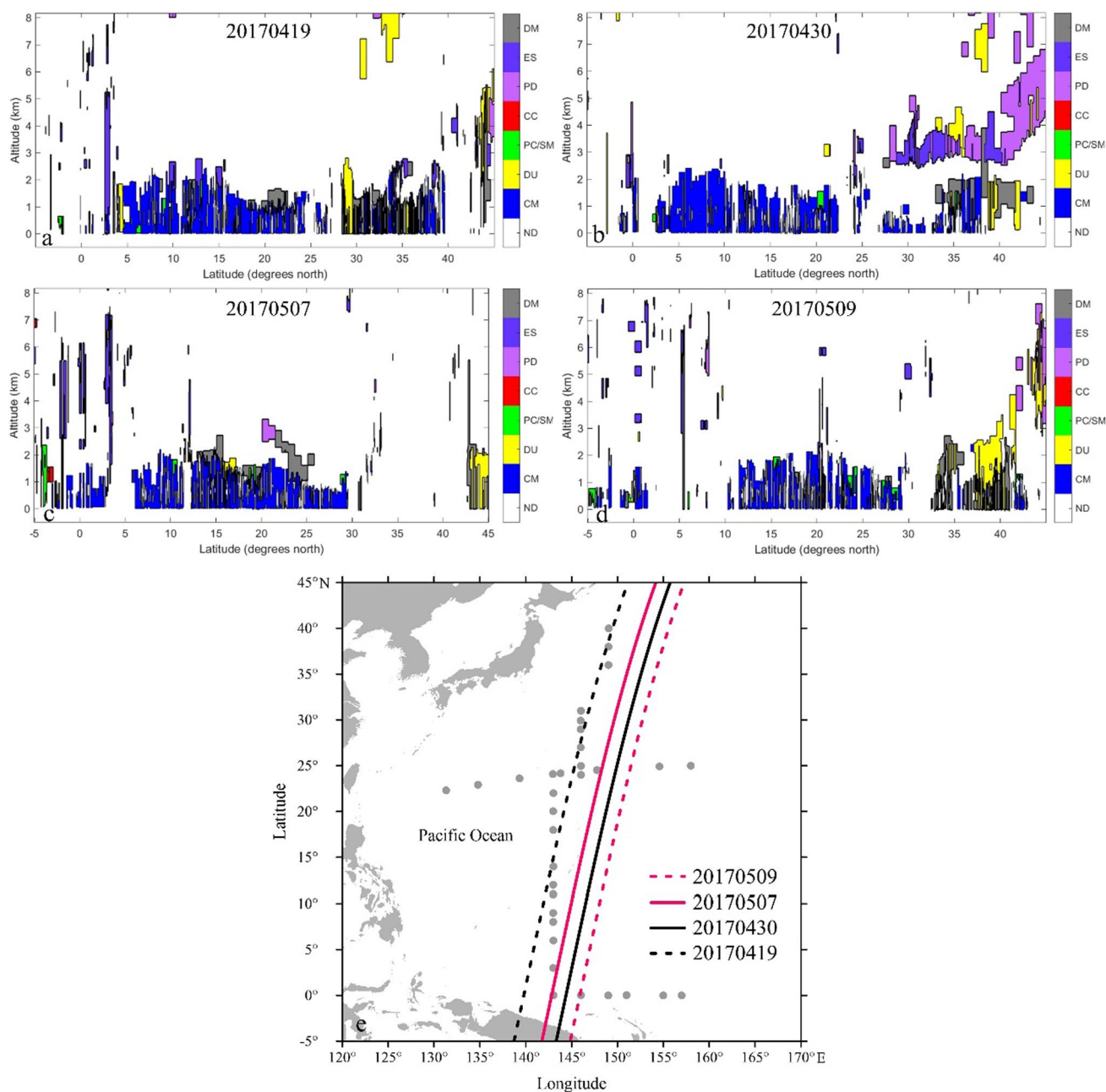


Fig. 5 a–d Vertical profiles of identified aerosol types (*ND* not determined, *CM* clear marine, *DU* dust, *PC/SM* polluted continental/smoke, *CC* clear continental, *PD* polluted dust, *ES* elevated smoke, *DM* dusty marine) along the orbits denoted in map (e)

latitude region. The higher SSA value at $0.4 \mu\text{m}$ near 0.975 (in Fig. 6) also confirms the presence of nonabsorbable particles, such as dust.

In comparison to section S1, section S2 mostly predominantly comprises clear marine-type aerosols. Only at specific latitudes, between 15 and 25 °N, are additional types of aerosols mixed under ambient conditions, such as dusty marine conditions. The dusty marine layers may be a combination of dust and urban pollution, according to the CALIOPSO classification, implying that the marine environment

in the region is still impacted by nearby terrestrial aerosols. A high concentration PM_{10} plume at 750–700 hPa is transported from Southeast Asia to the north of section S2 as a result of WRF-CHEM-simulated air pollution from 5 to 8 March 2017 proposed by Bagtasa et al. (2019). The notable reduction at $0.44 \mu\text{m}$ in the SSA spectrum also indicates the presence of maritime polluted aerosols.

CALIPSO contains a huge range of data with Not-Determined (ND) at the equator over the observation period. In Fig. 6, only four tracks with evident vertical distributions of

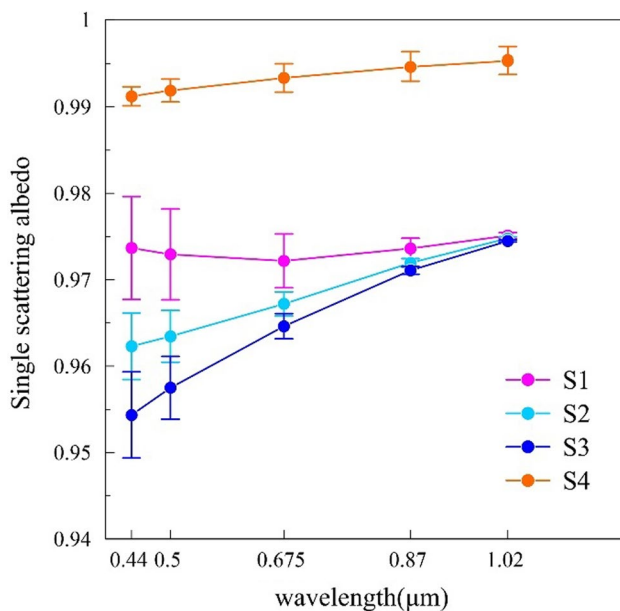


Fig. 6 The retrieved single scattering albedo for the four sections from the observation AOD using GRASP

aerosol types were chosen. The predominant aerosols around Papua New Guinea are clear-marine, elevated-smoke and polluted-continental/smoke types. Layers labeled as “polluted continental/smoke” in CALIPSO measurables can contain smoke, urban pollution or both types since it is not possible to unambiguously discriminate smoke from urban pollution. Figure 6 displays that the SSA is the smallest at 0.44 μm with an average value of 0.954, indicating the presence of absorbing aerosols under ambient conditions, which produces a rise in $C_{v,c}$.

Since S4 is a zonal section, CALIPSO operating meridionally cannot cover the whole section. Figure 6 displays that the SSA spectrum surpasses 0.99. Meanwhile, the lowest AOD indicates that it is pollution-free atmosphere. These evidences suggest that the aerosol over section S4 is not impacted by continental aerosols from East and Southeast Asia, and shows clear-marine type.

3.4 Potential sources of Aerosols over the Western Pacific Ocean

To evaluate the various sources of aerosol particles during the observation days, 120 h wind back trajectories were simulated using the HYSPLIT model. Figure 6a depicts the 120 h wind back trajectories associated with the observation days in April 2017 and Fig. 6b depicts the observation days in August 2019. Some differences in upwind source locations for the four sections can be inferred from the calculated trajectories.

In the north of S1 (> 35 °N), the wind trajectories of the three heights originate from westerly regions of northwest China and the Mongolian Plateau. However, in the south of S1 (25~35°N), air parcels at 2000 m and 5000 m primarily originate in East and South China or Southeast Asia. The particles in the surface layer are predominantly from the east of the observation area. The two stations north of section S2 (> 20 °N) are likewise impacted, with dusty marine aerosols detected in Fig. 5a and c.

The clear marine aerosol from the central Pacific is pushed south by the northeasterly wind to section S2 (0~20 °N), where the AODs are normally low and the aerosol is mostly Clear-Marine type (Fig. 5). The continental aerosol from Papua New Guinea has the greatest impact on section S3. Biomass burning for the purpose of land clearance is ubiquitous in the Southeast Asia (Duncan et al. 2003). The $C_{v,c}$ in this location is greatly increased by aerosols, urban pollution or both types delivered by the atmosphere.

Section S4 is in the center ocean and is only observed during summer. The HYSPLIT simulation results demonstrate that the particles at all sites except B1 originate from the open sea, and the measured AOD is lower than the ‘baseline’ of oceanic AOD. The aerosol at B1 may be tracked back to the South Asia due to the impact of the southwest monsoon. The observed AOD(500) at B1 is 0.26, which is the section’s highest value.

According to Wang et al. (2022), the seasonal north–south migration of the subtropical high is responsible for the seasonal fluctuation in AOD across the Western Pacific. The research includes observation data from spring to summer at the intersection of 25°N and 146°E, allowing us to investigate the seasonal change in aerosol characteristics. To illustrate the seasonal fluctuation, the wind back trajectory was simulated at the sites of 2019 using the meteorological conditions on April 20, 2017, as shown in Fig. 6b. The particles at the majority of sites can be traced back to Southeast Asia, which is notably different from that from the open ocean in August, 2019. The AOD (550) measured at A8 is double that of station B6. The direct radiative forcing effect of LRT aerosols was estimated using the Fu-Liou radiative transfer model at 25 °N, 145 °E. In comparison to the summer AOD baseline (AOD (550)=0.04), the projected net shortwave/longwave radiative effect of spring LRT aerosols (AOD (550)=0.09) at the sea surface is -3.1 W m^{-2} and -1.4 W m^{-2} , resulting in a net radiative effect of -1.7 W m^{-2} . In spring, the cooling impact is nearly 300% greater than that in summer (Fig. 7).

Recently, observations have shown that AOD (550) has gradually dropped in East Asia (Jin et al. 2019 018b; Wang et al. 2022). The ongoing reduction in aerosols implies that the cooling effect of aerosols on the sea surface is diminished, and their impact on the climate system warrants additional investigation.

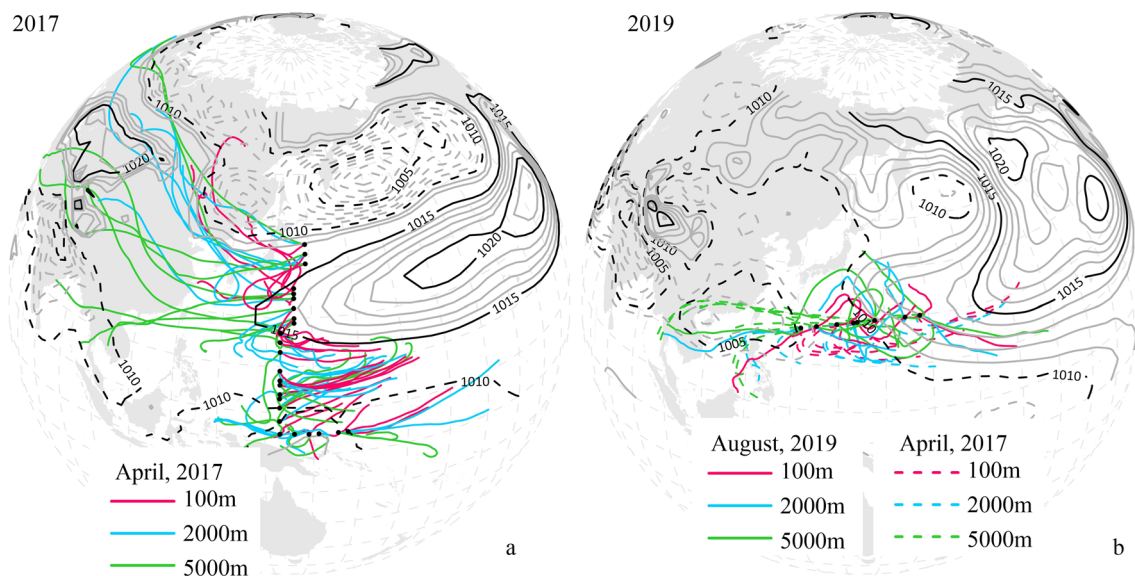


Fig. 7 120h wind back trajectory using HYSPLIT at 100 m, 2000 m and 5000 m before the observation days and composite monthly mean wind speed in April 2017 (a), and the comparison of 120 h wind back trajectory simulated by using the meteorological data on April

20, 2017 denoted by dashed lines with it before the observation days denoted by solid line (on August, 2019) (b). The isogram refers to the sea level pressure in April 2017 (a) and August 2019 (b)

4 Summary and discussion

The project ‘Global change and Air–Sea Interaction’ has conducted AOD observations in the western Pacific twice in April 2017 and August 2019. Observations have revealed a considerable north–south difference in aerosol properties over the western Pacific, including AOD, AOD spectrum and Angström exponent. According to the spatial distribution of AOD, the observation stations are categorized into four sections in the paper: a meridional S1 section in the north of 25 °N, a meridional S2 section in the south of 25 °N, a zonal S3 section at 0° and a zonal S4 section at 25 °N. In this paper, the GRASP inversion approach is used to derive the aerosol size distributions, and the HYSPLIT back trajectory mode is used to track aerosol particles from all sites. We focus on the north–south differences in aerosol volume size distribution, aerosol volume concentration, and aerosol type across the western Pacific Ocean.

In the Western Pacific, the resulting aerosol size distribution (normalized by aerosol volume concentration) is homogeneous and universal, with the primary variances across sites being in the coarse mode. The relevant parameters are essentially consistent with the aerosol size distribution under pure maritime conditions reported by Sayer et al. (2012). Section S1 has the highest computed fine mode aerosol volume concentration ($C_{v,f}$) with an average value of 0.0393, which is 4.5 times that of S2 and S3. Section S4 is located in the open water, and its average $C_{v,f}$ is smallest, reaching just 0.0046, which is only half of S2 and S3 sections and less

than the worldwide average value of 0.0053 published by Sayer et al. (2012). The combined analyses of atmospheric circulation patterns, backward trajectories, and remote sensing show that aerosols in high-latitude regions are affected by the dust climate in East Asia, and their types are diverse. The Clear-Marine aerosol from the central Pacific is delivered to the south to section S2 (0~20 °N) by the northeasterly wind. Clear aerosols of the elevated-smoke type are noticed in section S3 as a result of continental biomass burning, resulting in a remarkable rise in the coarse mode aerosol volume concentration ($C_{v,c}$).

Observations at 25 °N, 165 °E twice provide an opportunity to investigate seasonal changes in aerosol properties. A spring observed LRT high concentration PM₁₀ plume is observed from Southeast Asia. The measured AOD is double that in summer. However, we find a lower AOD in August than ever before in a pollution-free environment, with an AOD (550) of just 0.048. In comparison to aerosols in summer, the cooling impact modulated by aerosols in spring is roughly 300% stronger. Zhao et al. (2018a, b, c) found that warmer Arctic air temperature, which is inversely correlated with the loss of sea ice in the Arctic region, is correlated to the strengthening of the Siberian high. A stronger high leads to strong than usual winds in parts of China that strengthen the LRT transport in downwind regions. More LRT events may be expected as a result of climate change.

Furthermore, the resulting aerosol size distribution is unaffected by the measurement site, and the seasonal variance is rather subtle. The exceptional universality property

of aerosols suggests that they may be applied to aerosol models and satellite remote sensing applications over the Western Pacific. However, we need to pay attention to the large difference in aerosol particle volume concentration in practice, which is determined not only by wind, humidity, or water vapor content, but also by the LRT event.

Acknowledgements Thanks for funding from Global Change and Air-Sea Interaction II (GASI-01-NPAC-STsum) and Global change and Air-Sea Interaction I (GASI-02-PAC-STMSspr).

Data Availability the wind dataset at 10 m above sea level is available on the website: https://data.marine.copernicus.eu/product/WIND_GLO_PHY_L4_MY_012_006/description. The AOD data used in this paper can be shared if acquired by anyone.

Declarations

Conflict of interests Authors are required to disclose financial or non-financial interests that are directly or indirectly related to the work submitted for publication.

References

- Alizadeh-Choobari O, Sturman A, Zawar-Reza P (2014) A global satellite view of the seasonal distribution of mineral dust and its correlation with atmospheric circulation. *Dyn Atmos Oceans* 68:20–34. <https://doi.org/10.1016/j.dynatmoce.2014.07.002>
- Aoki K, Fujiyoshi Y (2003) Sky radiometer measurements of aerosol optical properties over Sapporo, Japan. *J Meteorol Soc Jpn* 81:493–513. <https://doi.org/10.2151/jmsj.81.493>
- Bagtasa G, Cayetano MG, Yuan CS et al (2019) Long-range transport of aerosols from East and Southeast Asia to northern Philippines and its direct radiative forcing effect. *Atmos Environ*. <https://doi.org/10.1016/j.atmosenv.2019.117007>
- Chen C, Dubovik O, Fuertes D, et al (2020) Validation of GRASP algorithm product from POLDER/PARASOL data and assessment of multiangular polarimetry potential for aerosol monitoring. *Earth Syst Sci Data* 12. <https://doi.org/10.5194/essd-12-3573-2020>
- Dubovik O, King MD (2000) A flexible inversion algorithm for retrieval of aerosol optical properties from Sun and sky radiance measurements. *J Geophys Res Atmos* 105:20673–20696. <https://doi.org/10.1029/2000JD900282>
- Dubovik O, Smirnov A, Holben BN et al (2000) Accuracy assessments of aerosol optical properties retrieved from Aerosol Robotic Network (AERONET) Sun and sky radiance measurements. *J Geophys Res Atmos* 105:9791–9806. <https://doi.org/10.1029/2000JD900040>
- Dubovik O, Holben B, Eck TF et al (2002) Variability of absorption and optical properties of key aerosol types observed in worldwide locations. *J Atmos Sci* 59:590–608. [https://doi.org/10.1175/1520-0469\(2002\)059%3C0590%3AVOAAOP%3E2.0.CO](https://doi.org/10.1175/1520-0469(2002)059%3C0590%3AVOAAOP%3E2.0.CO)
- Dubovik O, Herman M, Holdak A et al (2011) Statistically optimized inversion algorithm for enhanced retrieval of aerosol properties from spectral multi-angle polarimetric satellite observations. *Atmos Meas Tech* 4:975–1018. <https://doi.org/10.5194/amt-4-975-2011>
- Duncan BN, Martin R, Staudt AC et al (2003) Interannual and seasonal variability of biomass burning emissions constrained by satellite observations. *J Geophys Res*. <https://doi.org/10.1029/2002jd002378>
- Eck TF, Holben BN, Dubovik O et al (2005) Columnar aerosol optical properties at AERONET sites in central eastern Asia and aerosol transport to the tropical mid-Pacific. *J Geophys Res D* 110:1–18. <https://doi.org/10.1029/2004JD005274>
- Eck TF, Holben BN, Reid JS et al (2009) Optical properties of boreal region biomass burning aerosols in central Alaska and seasonal variation of aerosol optical depth at an arctic coastal site. *J Geophys Res* 114:1–14. <https://doi.org/10.1029/2008JD010870>
- Garrett TJ, Zhao C (2006) Increased Arctic cloud longwave emissivity associated with pollution from mid-latitudes. *Nature* 440:787–789. <https://doi.org/10.1038/nature04636>
- Han Z, Li J, Xia X, Zhang R (2012) Investigation of direct radiative effects of aerosols in dust storm season over East Asia with an online coupled regional climate-chemistry-aerosol model. *Atmos Environ* 54:688–699. <https://doi.org/10.1016/j.atmosenv.2012.01.041>
- Huang J, Fu Q, Su J et al (2009) Taklimakan dust aerosol radiative heating derived from CALIPSO observations using the Fu-Liou radiation model with CERES constraints. *Atmos Chem Phys*. <https://doi.org/10.5194/acp-9-4011-2009>
- Husar RB, Prospero JM, Stowe LL (1997) Characterization of tropospheric aerosols over the oceans with the NOAA advanced very high resolution radiometer optical thickness operational product. *J Geophys Res Atmos* 102:16889–16909. <https://doi.org/10.1029/96jd04009>
- Kaufman YJ, Smirnov A, Holben BN, Dubovik O (2001) Baseline maritime aerosol: Methodology to derive the optical thickness and scattering properties. *Geophys Res Lett*. <https://doi.org/10.1029/2001GL013312>
- Kaufman YJ, Tanré D, Boucher O (2002) A satellite view of aerosols in the climate system. *Nature* 419:215–223. <https://doi.org/10.1038/nature01091>
- King MD, Byrne DM, Herman BM, Reagan JA (1978) Aerosol size distributions obtained by inversion of spectral optical depth measurements. *J Atmos Sci* 35:2153–2167. [https://doi.org/10.1175/1520-0469\(1978\)035%3c2153:asdobi%3e2.0.co;2](https://doi.org/10.1175/1520-0469(1978)035%3c2153:asdobi%3e2.0.co;2)
- Lee SJ, Jeong YC, Yeh SW (2020) The lagged effect of anthropogenic aerosol on east asian precipitation during the summer monsoon season. *Atmosphere (basel)*. <https://doi.org/10.3390/atmos11121356>
- Li J, Han Z (2016) Aerosol vertical distribution over east China from RIEMS-Chem simulation in comparison with CALIPSO measurements. *Atmos Environ* 143:177–189. <https://doi.org/10.1016/j.atmosenv.2016.08.045>
- Li Z, Lau WKM, Ramanathan V et al (2016) Aerosol and monsoon climate interactions over Asia. *Rev Geophys* 54:866–929. <https://doi.org/10.1002/2015RG000500>
- Li L, Dubovik O, Derimian Y, et al (2019) Retrieval of aerosol components directly from satellite and groundbased measurements. *Atmos Chem Phys* 19. <https://doi.org/10.5194/acp-19-13409-2019>
- Li L, Derimian Y, Chen C, et al (2022) Climatology of aerosol component concentrations derived from multiangular polarimetric POLDER-3 observations using GRASP algorithm. *Earth Syst Sci Data* 14:3439–3469. <https://doi.org/10.5194/essd-14-3439-2022>
- (Lopatin A, Dubovik O, Fuertes D, et al (2021) Synergy processing of diverse groundbased remote sensing and in situ data using the GRASP algorithm: applications to radiometer, lidar and radiosonde observations. *Atmos Meas Tech* 14. <https://doi.org/10.5194/amt-14-2575-2021>
- Merkulova L, Freud E, Mårtensson EM et al (2018) Effect of wind speed on Moderate Resolution Imaging Spectroradiometer (MODIS) aerosol optical depth over the North Pacific. *Atmosphere (basel)* 9:10–14. <https://doi.org/10.3390/atmos9020060>

- Qiang Fu, Liou KN (1993) Parameterization of the radiative properties of cirrus clouds. *J Atmos Sci*. [https://doi.org/10.1175/1520-0469\(1993\)050%3c2008:potrpo%3e2.0.co;2](https://doi.org/10.1175/1520-0469(1993)050%3c2008:potrpo%3e2.0.co;2)
- Qiang-Fu, Liou KN (1992) On the correlated k-distribution method for radiative transfer in nonhomogeneous atmospheres. *J Atmos Sci*. [https://doi.org/10.1175/1520-0469\(1992\)049%3c2139:otcdmf%3e2.0.co;2](https://doi.org/10.1175/1520-0469(1992)049%3c2139:otcdmf%3e2.0.co;2)
- Ramanathan V, Crutzen PJ, Kiehl JT, Rosenfeld D (2001) Atmosphere: aerosols, climate, and the hydrological cycle. *Science* (1979) 294:2119–2124
- Rolph G, Stein A, Stunder B (2017) Real-time environmental applications and display sYstem: READY. *Environ Modell Softw*. <https://doi.org/10.1016/j.envsoft.2017.06.025>
- Román R, Antuña-Sánchez JC, Cachorro VE, et al (2022) Retrieval of aerosol properties using relative radiance measurements from an all-sky camera. *Atmos Meas Tech* 15. <https://doi.org/10.5194/amt-15-407-2022>
- Sakerin SM, Kabanov DM, Smirnov AV, Holben BN (2008) Aerosol optical depth of the atmosphere over the ocean in the wavelength range 0.37–4 μm. *Int J Remote Sens* 29:2519–2547. <https://doi.org/10.1080/01431160701767492>
- Sayer AM, Smirnov A, Hsu NC, Holben BN (2012) A pure marine aerosol model, for use in remote sensing applications. *J Geophys Res Atmos*. <https://doi.org/10.1029/2011JD016689>
- Smirnov A, Holben BN, Slutsker I et al (2009) Maritime aerosol network as a component of aerosol robotic network. *J Geophys Res Atmos*. <https://doi.org/10.1029/2008JD011257>
- Smirnov A, Holben BN, Giles DM et al (2011) Maritime aerosol network as a component of AERONET—first results and comparison with global aerosol models and satellite retrievals. *Atmos Meas Tech* 4:583–597. <https://doi.org/10.5194/amt-4-583-2011>
- Stein AF, Draxler RR, Rolph GD et al (2015) NOAA's hysplit atmospheric transport and dispersion modeling system. *Bull Am Meteorol Soc*. <https://doi.org/10.1175/BAMS-D-14-00110.1>
- Sun Y, Zhao C (2020) Influence of Saharan dust on the large-scale meteorological environment for development of tropical cyclone over north Atlantic Ocean Basin. *J Geophys Res* 125:1–14. <https://doi.org/10.1029/2020JD033454>
- Tian Y, Pan X, Yan J et al (2019) Size distribution and depolarization properties of aerosol particles over the northwest pacific and arctic ocean from shipborne measurements during an R/V xuelong cruise. *Environ Sci Technol* 53:7984–7995. <https://doi.org/10.1021/acs.est.9b00245>
- Torres B, Dubovik O, Fuertes D et al (2017) Advanced characterisation of aerosol size properties from measurements of spectral optical depth using the GRASP algorithm. *Atmos Meas Tech* 10:3743–3781. <https://doi.org/10.5194/amt-10-3743-2017>
- Twomey S (1977) The influence of pollution on the shortwave Albedo of Clouds. *J Atmos Sci* 34:1149–1152. [https://doi.org/10.1175/1520-0469\(1977\)034%3c1149:tiopot%3e2.0.co;2](https://doi.org/10.1175/1520-0469(1977)034%3c1149:tiopot%3e2.0.co;2)
- Wang Y, Fan S, Feng X (2007) Retrieval of the aerosol particle size distribution function by incorporating a priori information. *J Aerosol Sci* 38:885–901. <https://doi.org/10.1016/j.jaerosci.2007.06.005>
- Wang W, Zhu D, Jing C et al (2022) Spatial distribution and temporal variation of aerosol optical depth in the Western Pacific Ocean. *Dyn Atmos Oceans* 99:101303. <https://doi.org/10.1016/j.dynatmoce.2022.101303>
- Winker DM, Hunt WH, McGill MJ (2007) Initial performance assessment of CALIOP. *Geophys Res Lett*. <https://doi.org/10.1029/2007GL030135>
- Winker DM, Vaughan MA, Omar A et al (2009) Overview of the CALIPSO mission and CALIOP data processing algorithms. *J Atmos Ocean Technol*. <https://doi.org/10.1175/2009JTECHA1281.1>
- Yang Y, Zhao C, Wang Y et al (2021) Multi-source data based investigation of aerosol-cloud interaction over the north China plain and north of the Yangtze plain. *J Geophys Res*. <https://doi.org/10.1029/2021JD035609>
- Zhang XY, Arimoto R, An ZS (1997) Dust emission from Chinese desert sources linked to variations in atmospheric circulation. *J Geophys Res Atmos* 102:28041–28047. <https://doi.org/10.1029/97jd02300>
- Zhao C, Qiu Y, Dong X et al (2018a) Negative aerosol-cloud relationship from aircraft observations over Hebei, China. *Earth Space Sci* 5:19–29. <https://doi.org/10.1002/2017EA000346>
- Zhao S, Feng T, Tie X et al (2018b) Impact of climate change on siberian high and wintertime air pollution in China in past two decades. *Earths Future* 6:118–133. <https://doi.org/10.1002/2017EF000682>
- Zhao C, Yang Y, Fan H et al (2020) Aerosol characteristics and impacts on weather and climate over the Tibetan Plateau. *Natl Sci Rev* 7:492–495. <https://doi.org/10.1093/nsr/nwz184>

Publisher's Note Springer Nature remains neutral with regard to jurisdictional claims in published maps and institutional affiliations.

Springer Nature or its licensor (e.g. a society or other partner) holds exclusive rights to this article under a publishing agreement with the author(s) or other rightsholder(s); author self-archiving of the accepted manuscript version of this article is solely governed by the terms of such publishing agreement and applicable law.